Photonics **2014**, *1*, 303-322; doi:10.3390/photonics1040303

OPEN ACCESS
photonics
ISSN 2304-6732
www.mdpi.com/journal/photonics

Article

Infrared Retinoscopy

Ying-Ling Chen [1],*, Lei Shi [1],†, James W. L. Lewis [1] and Ming Wang [2]

[1] Center for Laser Applications, The University of Tennessee Space Institute, 411 B. H. Goethert Parkway, TN 37288, USA; E-Mails: lshi@utsi.edu (L.S.); jwllut@yahoo.com (J.W.L.L.)
[2] Wang Vision Institute, 1801 West End Ave, Ste 1150, Nashville, TN 37203, USA; E-Mail: drwang@wangvisioninstitute.com

† These authors contributed equally to this work.

* Author to whom correspondence should be addressed; E-Mail: ychen@utsi.edu; Tel.: +1-931-393-7448.

Received: 6 September 2014; in revised form: 29 September 2014 / Accepted: 30 September 2014 / Published: 3 October 2014

Abstract: Retinoscopy could be a more effective and versatile clinical tool in observing a wide range of ocular conditions if modifications were made to overcome the inherent difficulties. In this paper, a laboratory infrared retinoscope prototype was constructed to capture the digital images of the pupil reflex of various types of eye conditions. The captured low-contrast reflex images due to intraocular scattering were significantly improved with a simple image processing procedure for visualization. Detections of ocular aberrations were demonstrated, and computational models using patients' wavefront data were built to simulate the measurement for comparison. The simulation results suggest that the retinal stray light that is strongly linked to intraocular scattering extend the detection range of illuminating eccentricity in retinoscopy and make it more likely to observe ocular aberrations.

Keywords: retinoscopy; photorefraction; aberration

---

1. Introduction

Prior to the introduction of automated testing methods such as autorefraction, retinoscopy was the most practical objective method of measuring refractive status of an eye [1,2]. A classic spot retinoscope shines a spot of light into the patient's eye at a working distance that is normally between 1/3 and 2/3 of a meter, and the pupil reflex is observed. When moving the illumination across the eye, three types of reflex motions are observed: with-, against-, and neutral- respectively indicating a hyperopic-, a myopic-, and a null-refraction relative to the reciprocal of the working distance (in diopter = 1/m). Trial lenses are placed in front of the eye in order to reach the "neutralization" where a very bright reflex appears at centered illumination and disappears with a slight eccentricity in any side. Although retinoscopy is generally practiced for refraction determination, experienced clinicians are aware of its sensitivity in observing a variety of ocular conditions including irregular astigmatism or high-order aberrations [3–5]. One such example is the "scissor movement" or "split reflex" observation in keratoconus cornea dystrophy. However, drawbacks to the use of this versatile tool include the facts that first, its bright visible illumination in the extensive examination could be uncomfortable to examinees; it also causes the pupil to contract, and as a result, the use of eye drops for pupil dilation is often required; second, the broad-spectrum light source mixes chromatic signals that results in a decrease of image contrast and measurement sensitivity. Further, retinoscopic observations of unusual ocular conditions are not registered in digital form for future reference, discussion, sharing, or review, and their use for validation with theoretical analysis.

Photorefraction (PR) is also an objective refraction-measurement technique that was introduced in the early 1980s [6–9]. Eccentric photorefraction (EPR) is the most commonly practiced PR technique today. EPR uses a camera to photograph the retinal reflex that is induced by a light source located on the side of the camera lens. EPR shares the similarity in its optical illumination and detection paths with a traditional spot retinoscope. Because of EPR's low demand on cooperation and eye alignment of the examinee, it has been widely used in screening preschool children for binocular refractive errors. Taking the advantages of PR's friendly nature and digital registration and including additional modifications, an infrared retinoscope could overcome the difficulties of the traditional retinoscope.

Illustrated in Figure 1a is the simple diagram of a traditional spot retinoscope (not to scale). Figure 1b shows the infrared retinoscope that is modified from EPR technique. The use of infrared sources and camera makes non-mydriatic measurements feasible for larger pupillary coverage and lessens the discomfort during measurement. The employment of a beam splitter and a 2-dimensional light source array that is aligned to the entrance pupil of the camera enables the detection of both coaxial and multiple eccentric and meridian reflex images just as the retinoscope does.

In this work, to test the sensitivity of observing abnormal ocular conditions we constructed a laboratory device with a simple 13-infrared LED array and used a near-working distance of 30 cm, which is a typical near-range that corresponds to a neutralization of −3.3 diopters. The experiment was performed as an additional test in a clinical setting where routine clinical diagnostics and treatments were given. The testing results were compared to the patients' clinical diagnostics and history. To investigate how ocular aberrations and other ocular conditions could affect the reflex images, we used the existing clinical wavefront aberration data to construct simple eye models and used the geometric image analysis in ZEMAX to reproduce the measurements for comparison.

Figure 1. Comparison of optical arrangements (not scaled) in (**a**) retinoscope, and (**b**) infrared retinoscope using multi-eccentric-meridian photorefraction design.

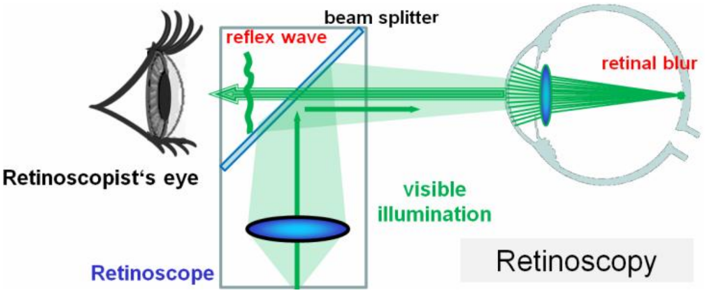

(**a**)

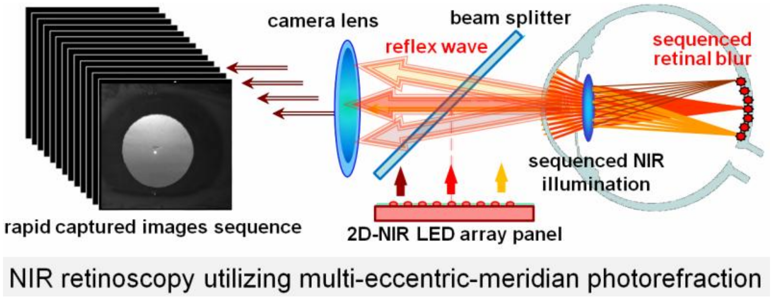

(**b**)

2. Theoretical Consideration

The intensity profiles of the reflex images in both photorefraction and retinoscopy are produced due to the fact that only a portion of the double-pass reflex at the pupil plane are detected by the PR camera or the peephole of the retinoscope. The portion of selection depends on how the returning reflex waves at the eye's exit pupil propagate to the detection plane; specifically, divergent as in a hyperopic eye or convergent as in a myopic eye. The retinoscope involves multiple optical apertures in both the illumination and the returning path that results in an unexpected "edge" complication in the formation of the reflex patterns [4,5]. The theoretical consideration of EPR is more straightforward without the edge/vignetting problems.

Figure 2 shows an illustration of an EPR setup. The system axis is aligned to the center of the camera's entrance pupil, and the coaxial or eccentric light sources are placed at the detection pupil plane with eccentricities ($\rho = 0$) and ($\rho = \rho'$) from the axis. Under neutralization condition, the light source plane conjugates to the retinal surface of the examined eye. The out-going reflex rays return to the originating light source. Therefore, as observed in the retinoscopy neutralization condition, a coaxial PR reflex image is a pupil image at maximum brightness and an eccentric reflex image is all dark since the light source is outside the detection area. When defocus or any aberration is present, the reflex wavefront still propagates toward the originating light source, but at the detection plane, the wavefront surface will extend over the area of the originating light source. Assume that the double-pass wavefront of an eccentric-meridian illumination at the polar axis coordinate (ρ', φ') is identical to that of a coaxial illumination at ($\rho = 0$) except for the direction of propagation. In this case, the camera lens would capture the wavefront portion centered at $(\rho, \varphi + \pi)$; *i.e.*, the opposite side of the light source. In Figure 2, the coaxial detection of an eccentric illumination from the lower side of a camera pupil is equivalent to a coaxial illumination with the eccentric detection on the upper side. Since the reflex photograph is imaged with focus on the eye's exit pupil plane, the intensity level at y'_1, y'_2, and y'_3 locations (photograph image at left of the figure) would be determined by the collected ray intensities toward this eccentric pupil at the upper location $(\rho, \varphi + \pi)$, originating from y_1, y_2, and y_3 at the eye plane, which are maximized at their wavefront surface normals. This is similar to wave aberration's first-order partial derivative that is used by Caballero to describe higher-order aberrations in PR [10]. In the case of a hyperopic eye that produces a divergent out-going wavefront, the collected rays at the upper side of the axis are therefore attributed to the upper portion of wavefront at the eye's exit pupil. This produces an upper crescent reflex image, which is opposite to the light source location at lower side. When moving the light source from the far lower side of the camera, passing the center, toward the upper side, the movement of the "crescent" reflex appears to be "against motion" in an hyperopic and "with motion" in a myopic eye, respectively, in the EPR-modified retinoscope.

The geometric theorems of EPR's crescent reflex early on use only the eye's pupil size, defocus, and the eccentricity measured from edge of light source to the edge of detector to determine their relationships to the reflex crescent boundary [7,8]. Other EPR approaches use slope-based analysis with the design of extended light sources [11]. Our previous study shows that the crescent edge could not be clearly defined when considerations of normal ocular aberrations and the detection pupil's size and shape are included [12]. Further, the intraocular scattering and retinal reflectance, which vary with age, race, and among individuals, produce a significant background signal that demands individual calibration to yield reliable measurements. However, unaffected by individual ocular variables in the PR image is the maximization of reflex intensity when approaching the neutralization, which is the way the trial lens is used in the classic retinoscopy. By utilizing a beam splitter as shown in Figure 1b and a Badal lens system, the optimal compensation power could be obtained to reach neutralization in one rapid PR imaging sequence. EPR image intensity also reduces with the increase of eccentricity. Along an arbitrary meridian, the reflex intensity produces a bell-shape curve peaked at the coaxial $(\rho = 0)$ location. The width of the bell curve increases with defocus. The 2-dimensional intensity surface $I(\rho, \varphi)$ could be described with an elliptical surface fitting with three variables, the maximum and minimum widths on two perpendicular meridians and the rotation of the ellipse. The astigmatic meridians could be determined without influence from individual ocular intraocular scattering, retinal reflectance, and pupil variables.

In a particular example of a high-order aberration keratoconus case with the red curve wavefront and wavefront normals illustrated in the right side of the figure, representing a bulging "cone", the reflex image on the left shows, respectively, the corresponding dark, bright, and deep dark at y'1, y'2, and y'3. By using a beam splitter and 2-dimensional array of light sources, the entrance pupil of camera becomes multiple spatial filters that sample the wavefront profile through the space—much like a cookie cutter sampling a piece of dough. The total double-pass wavefront normals at every pupillary location (x,y) could be determined from the related brightness in sampled multi-eccentric-meridian reflex images.

Figure 2. Illustration of the eccentric photorefraction detection of double-pass wavefront.

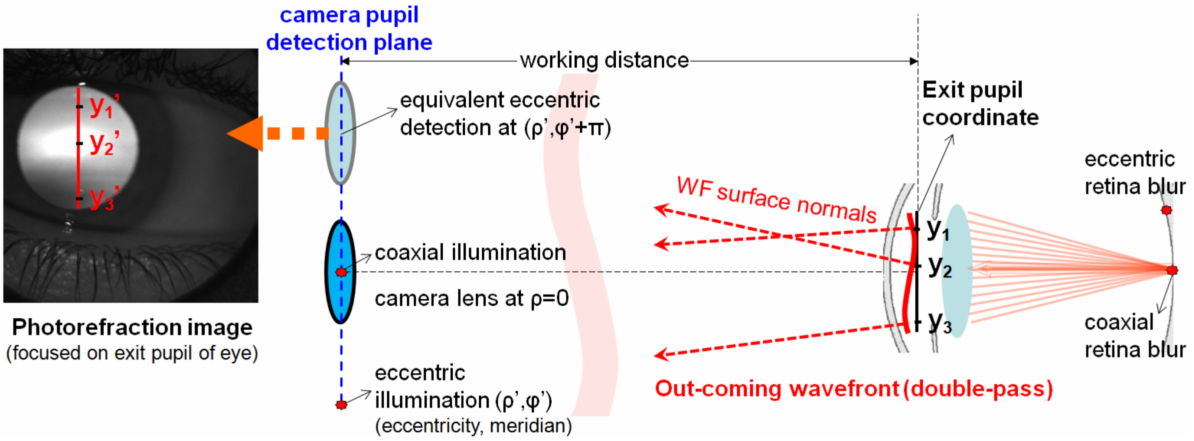

3. Experimental Section

3.1. Optical Components

The experimental prototype is the modified infrared photorefraction with a two-dimensional LED panel. The component arrangement is shown in Figure 1b (not-to-scale). The working distance from the eye location to the entrance pupil of the camera is 30 cm. The infrared camera lens is focused on the pupil of the eye. The LED panel consists of 13 NIR LEDs that are arranged in four meridians as shown in Figure 3. Each LED is about 6 mm with a 5 mm-diameter radiating field size. The light source at this size and working distance is considered as an extended source (~17 mradian). The LEDs radiate at wavelength 805+/−25 nm with maximum continuous output of 38 mW. During the measurements, the radiation of each LED pulse is limited between 10 and 50 ms. A feedback loop is programmed to control the LED's radiation pulse duration and the camera gain to prevent saturation or under exposure. All 13 LEDs are pulsed on in a rapid sequence as the camera captures the pupil reflex images. The camera frame rate is 120 Hz, but the maximum acquisition rate is dominant by the required exposure time, which is equal to the radiation pulse. Each monocular image (10-bit gray level) is 350 by 350 pixel in size. A 25R/75T pellicle beam splitter is used to align the LED panel image to the camera entrance pupil plane. After reflected from the beam splitter, the maximum use of the light emission is considered as minimal risk at the maximum accessible emission of 0.041 $j/cm^2/sr$, less than 1% of the emission limit according to the federal regulation, e-CFR 1040. The entrance pupil radius of the camera is set at 6 mm as marked in red dashed lines in Figure 3. With the intention to better observe various ocular abnormalities, this arrangement provides a coaxial illumination at the center, 4 knife-edge illumination at 0 and 90 degree meridians, and at 45 and 135 degree meridians with four EPR illuminations that are half-way overlapped by the detection, and four EPR illuminations that have no overlap area with the detection pupil. No mechanical or electronic approach for neutralization was constructed in this prototype.

Figure 3. The spatial arrangement of two-dimensional LED panel that contains 13 LEDs: one coaxial LED at the center surrounded with 12 eccentric LEDs. The red dashed line indicates the location of the projected entrance pupil of the camera.

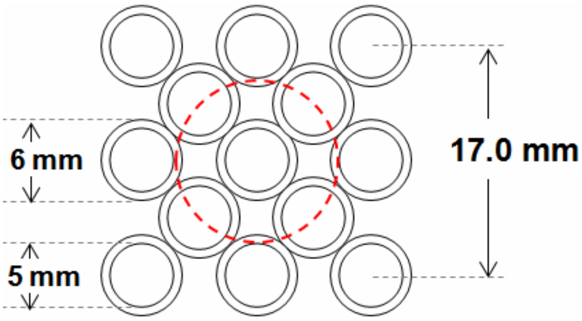

3.2. Clinical Testing

A total of 90 adult patients of Wang Vision Institute in Nashville participated in the experiment of the monocular infrared retinoscopic device during their visits for eye care. The experimental test was a voluntary addition that did not affect any clinical decision for their eye care. The IRB approval was obtained in the University of Tennessee at Knoxville. Prior to the tests the testing procedure, safety, and confidentiality were described to the participants and the signed consent forms were acquired. The measurements were performed when the room light was turned off. Once an eye was placed on the location and the camera detected the reflex, it automatically adjusted the radiation duration (10–50 ms) for optimal exposures and it acquired a sequence of images automatically. The patient only saw the blinking dim LED lights at 30 cm in front of the eye. The measurement for each eye took no longer than 3 s. All images were collected without difficulty. The clinicians who made the diagnosis and treatments were blinded to the IR retinoscopy findings.

For comparison, only the existing clinical data from the testing day and before were collected. The patients' clinical diagnostics data were de-identified except for a number that linked to the corresponding images. Over half of the eye images were acquired from normal eyes of subjects seeking refraction corrections (*i.e.*, spectacles, contact lens, or surgical corrections) or returning for follow-up examinations after treatments. Fifty-nine eyes in the 180 were clinically identified as keratoconus. The remaining non-infectious eyes presented with various ocular conditions. They included dry eyes, blepharitis, Fuch's endothelium dystrophy, and corneal scars, *etc.*

3.3. Computation of the Measurement

Computational models are useful to validate theory, and to investigate and evaluate influential ocular properties in the measurements. Existing wavefront aberrometry data from some of the participating eyes were available. These wavefront data allowed us to perform a computational study of the aberration reflex profiles. Using the optical design program, Zemax (Radiant Zemax, Redmond, WA, USA), a simple paraxial ideal lens eye-model was constructed with a Zernike phase plate that characterizes the patient's clinical wavefront aberration measurement. The optical components of the retinoscope prototype were constructed with the simple eye model. The geometric image analysis in Zemax was used to compute the retinal blur and to simulate the PR images. The Zernike phase plates were assumed for both inward and backward eye models. Spatial cares were taken to ensure the correct coordinate was obtained transferring between the two sequential computations, the Zernike coefficients' sign change in the two coordinate systems, wavelength correction and input-order of the Zernike coefficients from clinical data in line with the Zemax convention.

4. Results and Discussion

4.1. Unprocessed Infrared EPR Images

Shown in Figure 4 are some of the unprocessed infrared images obtained from the measurements. Tear-film breakup and debris/roughness of corneal surface were photographed in Figures 4a-4d. Image of Figure 4a was from a long-term contact-lens wearer's clinically normal healthy eye and the image was taken shortly after the removal of the contact lens. Figure 4b shows tear-film breakup in a normal healthy eye. Figure 4c was acquired from a dry-eye patient.

Images in Figures 4d−4f show eyes with various types of ophthalmic treatments or vision corrections. Figure 4d was from a healthy eye with implantable contact lens, one type of intraocular lens (IOL). Similar tear-film breakup ripples were observed in this picture. Figure 4e was from a healthy eye 24 years after a successful PK procedure. Figure 4f was taken from a keratoconus eye 16 days after the Intacs rings incision surgery.

Figures 4g, 4h, and 4i are example images of eyes with different types of diseases. Figure 4g is an eye with anterior basement membrane dystrophy (ABMD). Figure 4h is an eye with mild cortex cataract. From the comparisons between the 13 pictures with different illumination angles of the same eye, these two cases were illustrated most clearly on their coaxial images, and the image appearances were similar to the retroillumination in the slit-lamp observation.

Figure 4i was an eye with Fuch's endothelium dystrophy photographed by the far-eccentric illumination.

Between the 13 images, one could identify that some of the optical defects were captured by camera with their direct back-scattered light that is most vivid in the far-eccentric photorefraction images; image of Figure 4i is one of such case. Some other optical defects were seen most clearly in the knife-edge EPR detection. Unlike small optical defects with high spatial frequencies, ocular aberrations, which are described up to typically 7th-order in Zernike coefficients, in the photorefraction images appear as shadows or intensity gradient variations across the pupil reflex such as what were shown in the background of small defects in images of Figures 4a–4f. This aberration appearance is especially obvious in the keratoconus case in Figure 4f.

Transient optical defects such as tear-film problems and floaters can be differentiated from steady optical defects like cataract or corneal scars with comparison between two separate measurements.

Figure 4. (**a**) An image of an eye of a long-term contact-lens wearer. The image was taken shortly after the daily wear contact lens was removed. (**b**) Tear-film breakup image of a normal eye. (**c**) Image from a dry eye patient. **(d)** Image of a healthy eye with implantable contact lens. Tear-film breakup is also observed. (**e**) Image from a healthy eye with PK performed 24 years before. (**f**) Image of a keratoconus eye 16 days after Intacs surgery. (**g**) Image of an eye with anterior basement membrane dystrophy (ABMD). (**h**) Image of an eye with mild cortex cataract. (**i**) Image of an eye with Fuch's endothelium dystrophy. In each image, the white dot near the center of pupil reflex is the corneal reflection, the first Purkinji image.

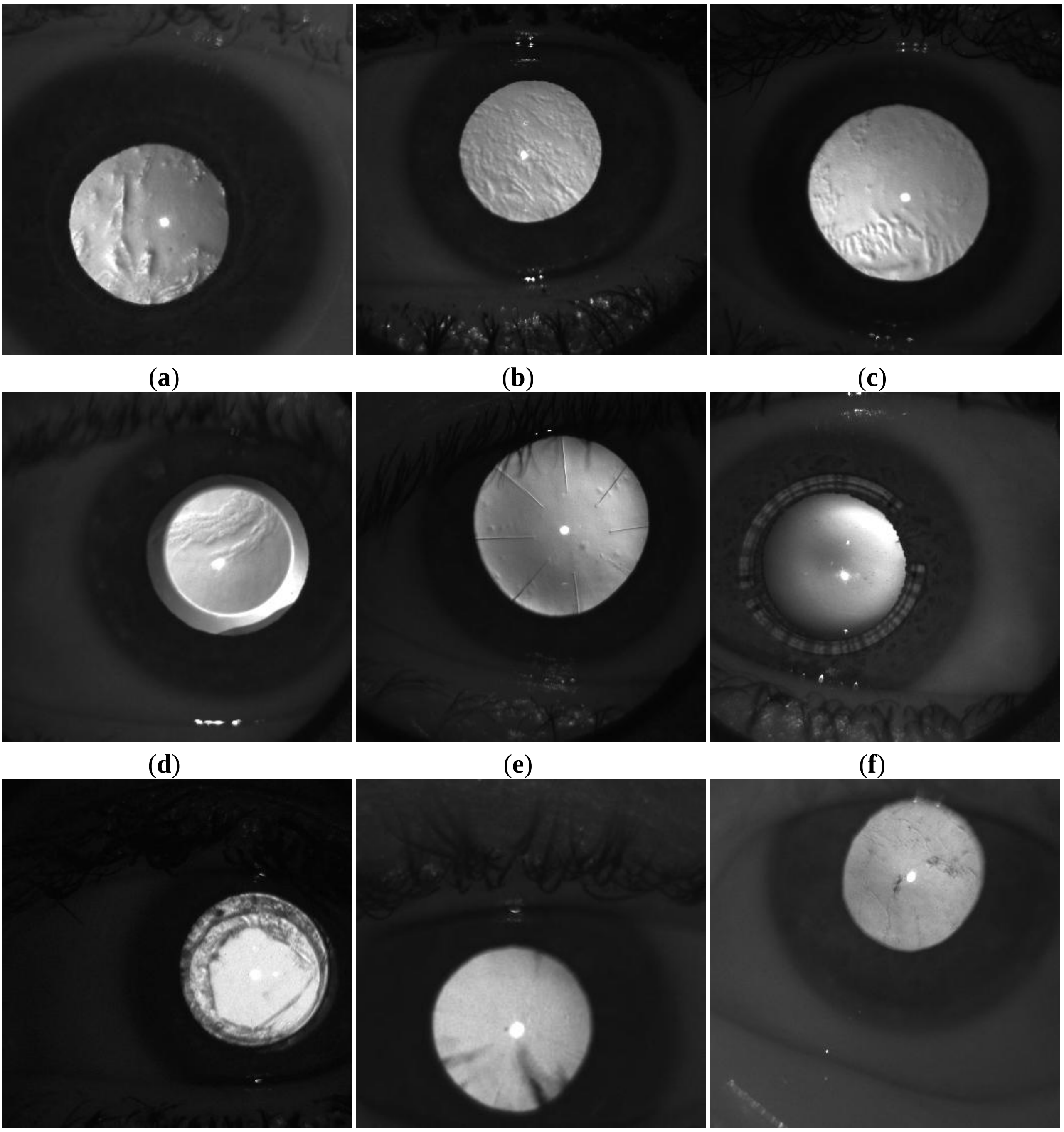

(**a**) (**b**) (**c**)

(**d**) (**e**) (**f**)

(**g**) (**h**) (**i**)

4.2. Refractions

Both high-order and low-order ocular aberrations in the retinoscopy are observed in the movement of the pupil reflex pattern when the illumination moves across different meridians and eccentricities. For simple visualization, the circular pupil reflex areas of the acquired 13 photorefraction images were identified automatically, cropped, and combined according to their illumination eccentricities-meridian (ρ, φ) position using a custom-built image analysis program in Matlab. To increase the contrast of visualization, simple image processing algorithms were applied: First, each gray-scale image is automatically rescaled from its own maximum to minimum intensity. The gray level 13-image maps are shown in the left side of Figure 5 for selected cases. Next, for the experimental image data, the corneal reflection, the first Purkinji image, is identified, removed, and refilled with ambient intensity. Finally, the histogram equalization, a typical image analysis process, was applied to the pupil reflex and the gray levels were colored from "hot to cold" accordingly. This step prevents the extreme intensity signals in small numbers of pixels resulting from optical opacities or reflectors from burying the aberration reflex pattern. The colored 13-image maps are shown in the right side of Figure 5 for selected cases in comparison. All image processing procedures were performed automatically with the code without manual manipulation.

The following sections describe the final results for different types of ocular aberrations.

4.2.1. Defocus

The eccentric photorefraction pupil reflex image has been demonstrated as a crescent or slope along the eccentricity direction. The direction of the crescent indicates far- or near-sightedness. For normal eyes with spherical defocus, the 13-image maps appear as rotationally symmetric form.

Presented on the left of Figure 5 are the assembled gray-scale images and on right are their corresponding color-coded images. Images of Figure 5a were acquired from a healthy plano, 20/20 eye seeking presbyopia correction. The gray-scaled images show no optical defects like those in Figure 3. When viewing a line of reflex images along an arbitrary meridian, for example, the five reflex images at 45 degree meridian from the top right to the lower left, the brightness appearance emerges "against the motion" that is similar to the spot retinoscope observation. This hyperopic appearance is presented because the emmetropic eye is on the hyperopic side relative to the neutralization refraction, which is located at −3.3 diopters.

Images in Figure 5b were acquired from a normal myopic eye with manifest refractive error and best corrected visual acuity (BCVA) of −6.25DS + 0.75DCX075 and 20/25, respectively. As the gray-scale map on the left shows, the gradient intensity variations in many images are fairly flat. This could be a result from the intraocular scattering. The color map on the right shows clearly the photorefraction crescent or slope direction in each image and the assembled map demonstrates a well-defined rotationally symmetric pattern with outward brighter features. Along any of the four meridians in this map, the reflex resembles the "with the motion" behavior of a spot retinoscope.

Figure 5c was a second measurement acquired from the same eye in as in Figure 5b while the tear film breakup occurred. Emerging from the wobbly or wavy background is the same color map showing that the high spatial frequency noise does not affect the low-order aberration reading. The repeatability of measurements of non-transient, low spatial frequency optical defects was encouraging for the technique.

Figure 5. (**a**) Image acquired from the left eye of a 47 year-old Caucasian female seeking presbyopia correction. The center reflex image in the 13-image map is the coaxial image. The eye is 20/20 with no correction (plano). The gray-scaled images show no optical defects. When viewing a series of reflex images along an arbitrary meridian, the brightness appearance emerges "against the motion" that is similar to the spot retinoscope observation. (**b**) Image acquired from an eye with refractive error and BCVA are −6.25DS + 0.75DCX075 and 20/25, respectively. The color map on the right demonstrates a well-defined symmetric pattern with outward brighter features, and this resembles "with the motion" behavior of the spot retinoscope of myopia. (**c**) Image acquired from the same eye in (b) while the tear film breakup occurred. Emerging from the wobbling, wavy background is the same color map showing that the noise from high spatial frequency does not affect the low-order aberration reading.

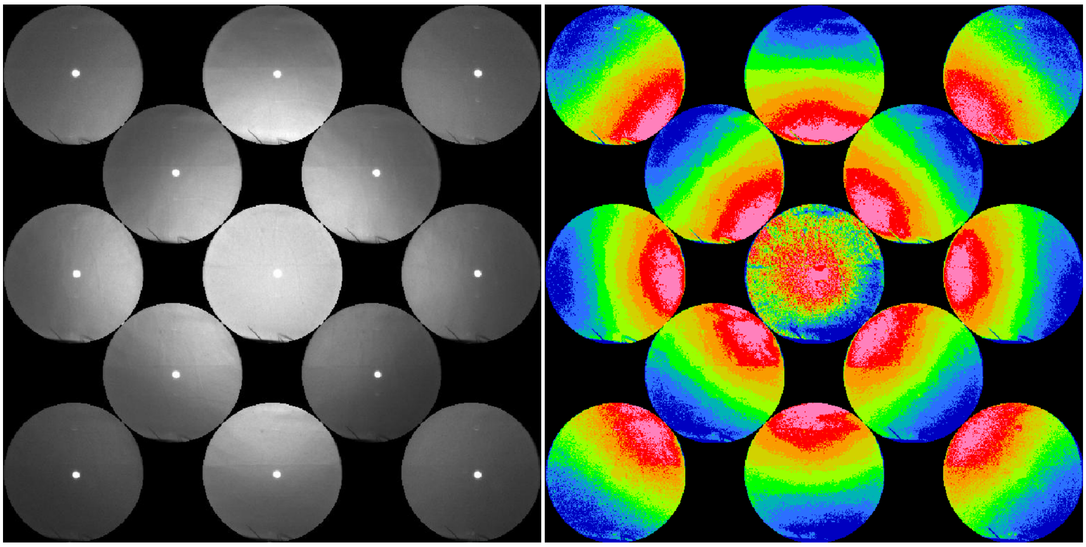

(**a**)

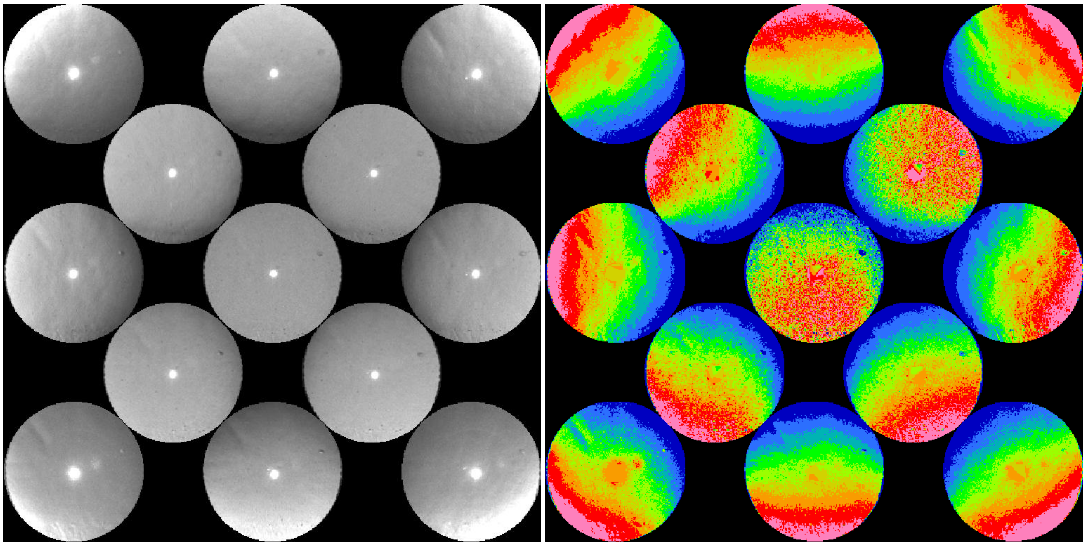

(**b**)

Figure 5. *Cont.*

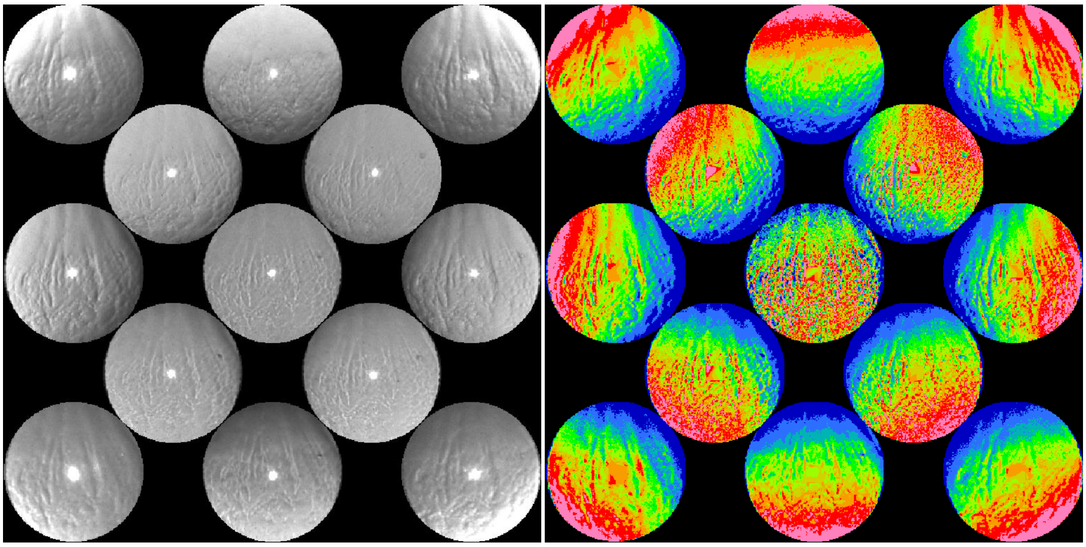

(**c**)

Figure 6. Computational result of the measurement of the eye in Figure 5b and c. No accommodation was applied. Intraocular scattering was applied to produce the outer eccentric images.

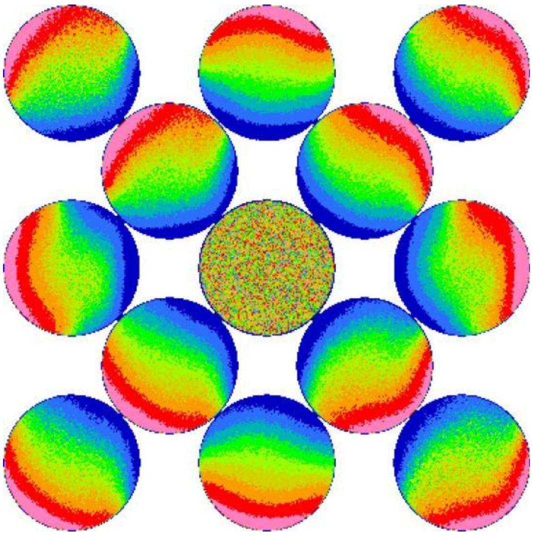

Shown in Figure 6 is the simulation result using the wavefront data acquired from the same eye of Figure 5b and c. The white background is used to distinguish the computation result from the experiment color map. While this computational result appears to show good agreement with the experiment images, only the center five images were produced with the retinal blur or the point spread function that was obtained by ray tracing in the illumination path. The far-eccentric photorefraction images in the four corners could not be produced without extending the retinal blur size by almost a factor of three. The four knife-edge EPR reflex images at 0 and 90 degree meridians would also be truncated if the retinal blur size were not increased by about 50% in the computation. The existence of intraocular scattering or the internal reflection in the multi-layer retina could significantly extend retinal blur coverage or retinal stray light as described by van den Berg [13]. Intraocular scattering has been long observed as a significant background signal in the photorefraction, retinoscopy, and any ophthalmic devices using double-pass signals. The experiment and the computational comparison in Figures 5 and 6 suggest that the retinal stray light must play a role to allow the far eccentric PR images to be present.

4.2.2. Astigmatism

Similar to spherical defocus, one may expect that the existence of astigmatism transforms the rotational symmetry in the color map into an elliptical symmetry along the two principal meridians. Figure 7a shows results from two cases of astigmatic eyes: on the left is an eye with a high degree of spherical defocus (related to the neutralization of −3.3 diopters). On the left is an astigmatic eye with relatively lower defocus related to −3.3 diopters. When the refractive error is close to neutralization, the coaxial reflex intensity is at its highest and the intensity levels of the eccentric reflex image are low, thereby resulting in grainy boundaries between colors. On the other hand, the reflex image has sharp boundaries when refractive error is relatively high. This is shown in the two eyes in Figure 7a. The high hyperopic astigmatism was obtained from an eye with the manifest refraction of +3.50DS + 3.75DCX110. At the detection plane, the divergent wavefront is expanded by the related defocus of +6.8 diopters at the 110 degree meridian and + 10.55 diopter at the 20 degree meridian and had an elliptic shape wider at 20 degree. The coaxial detection collects a circular sample at the center of this ellipse, and the reflex image shows a clear ellipse from the eye's pupil plane with axes aligned to 11 degrees, the axis with lower refractive error. The astigmatism condition as manifested by the elliptically shaped contours can also be observed from the eccentric images that surround the coaxial images, especially at the 45 and 135 degree meridians.

Shown in the right side of Figure 7a is an image obtained from an astigmatic eye that has a manifest refraction of −2.75 + 2.75X165 (20/20). Because of the relatively low spherical defocus of ~0.5 diopter (related to neutralization) along the 165 degree meridian, the crescents reflex patterns of the horizontal PR images that are nearly unrecognizable due to low intensity. However, at the vertical 90 degree meridian, the hyperopic crescents are clear. The far eccentric PR images also clearly form the elliptical appearances.

Figure 7b shows a result of non-elliptical appearance of the astigmatic condition. This happens −refractive errors, or the crescent directions, along the two astigmatic principle meridians lay on opposite sides. As a result, the eye images appear brighter along the outward direction (with the motion) on the vertical meridian; *i.e.*, more myopic than the neutralization. The image intensity behaves oppositely in the horizontal meridian where the measured power is less myopic than the neutralization. In the 45 degree and 135 degree meridians, the reflex images appear as merged or combined images of the two neighboring images. Although each of the 12 eccentric images still appear as the crescent or slope reflex image, the combined color map does not exhibit or resemble rotational symmetry. Instead, the color map forms a somewhat “X- shaped” figure.

For the simulation work, unfortunately, we do not have the wavefront data for the eye in Figure 7b. Another eye with refractive prescription of −4DS + 1.75DCX82 (20/20) was used for the computation. The refractive defocus at 82 degrees is slightly more myopic than −3.3 diopter and the defocus at 172 degrees is hyperopic. Figure 8 illustrates the comparison between (a) the computational result and (b) the experiment testing result of this eye. From both of the experiment measurements and the simulations, the two principal meridians at ~82 degrees that are myopic with motion and ~172 degrees that are hyperopic against motion are clearly seen. Again, in the simulation, the extension of retinal blur from the retinal stray light was required to produce the pupil reflex image in the outlying eccentric photographs.

Figure 7. (**a**) Color maps of a relatively high hyperopic eye (left) and a less hyperopic astigmatic eye (right). Manifest refractions of the two eyes are measured as +3.50DS + 3.75DC X110 (20/30) and −2.75DS + 2.80DC X165 (20/20), respectively. (**b**) Measured image of an interesting case of astigmatic eye with dry eye syndrome. The refractive errors appear to be myopic along one principal meridian and hyperopic along the other principal meridian. The spherical equivalent falls right on the neutralization refraction.

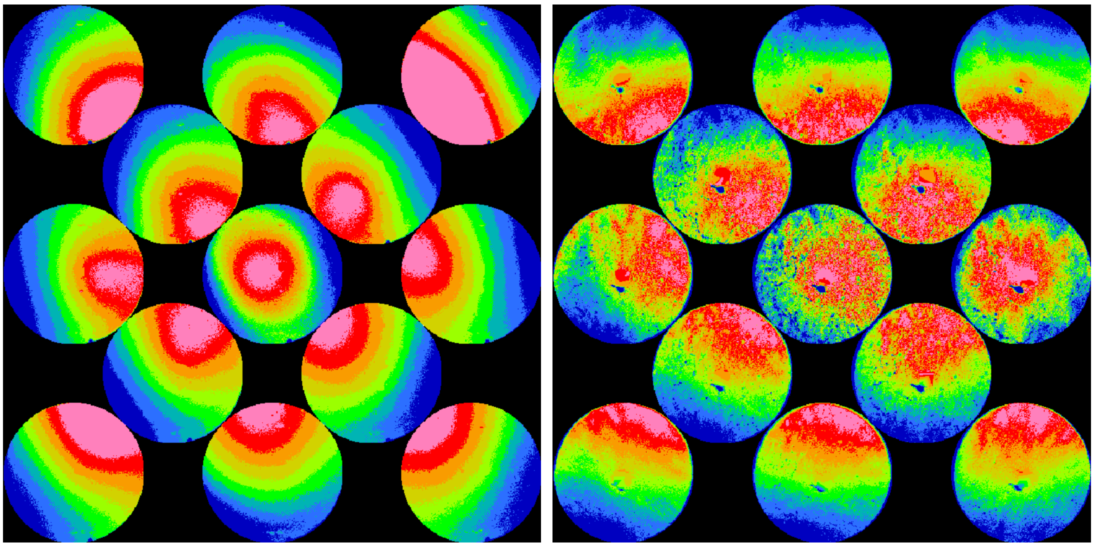

(**a**)

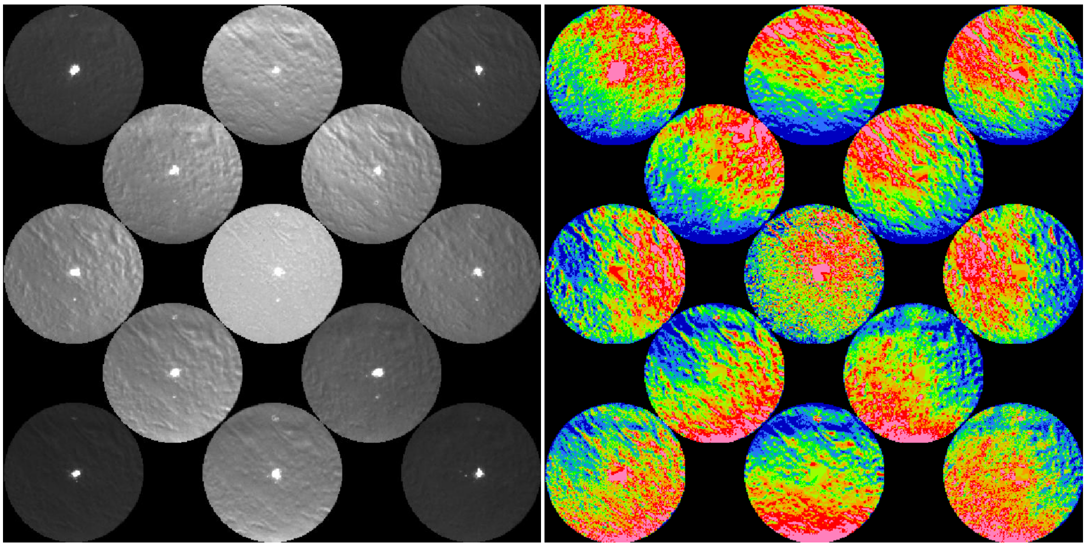

(**b**)

Figure 8. Comparison between (**a**) the computational result of an astigmatic eye with refractive error along the two principal meridians fall on either side of the neutralization (−3.3D). The manifest refraction of this eye was measured as −4DS + 1.75DCX82 with BCVA of 20/20, and (**b**) the experiment testing result of the same eye.

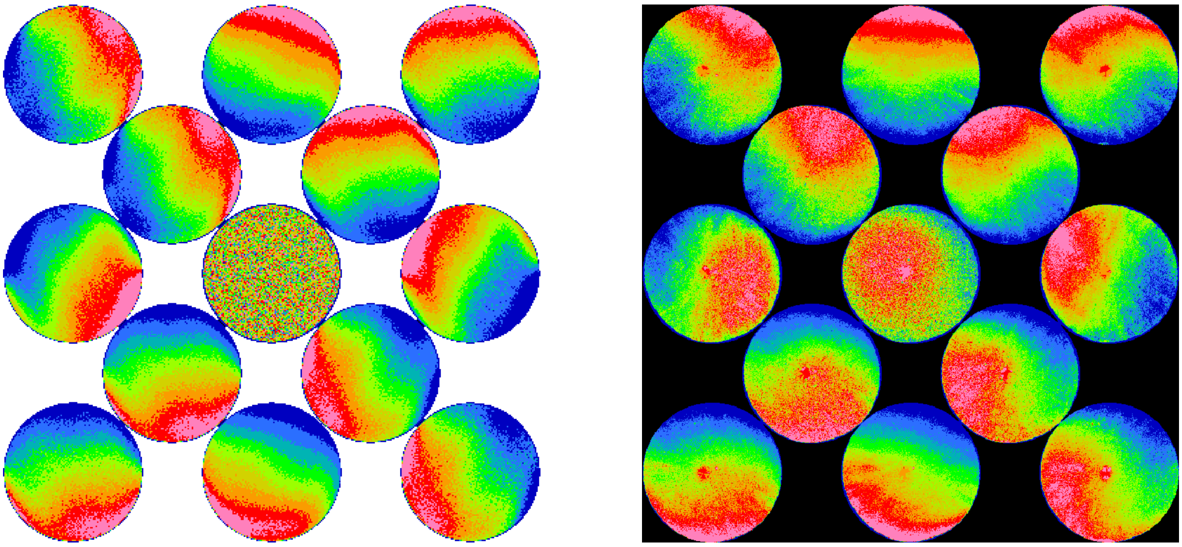

(**a**) (**b**)

4.3. High-Order Aberration

The measurements of keratoconus eyes provide the insight to the retinoscopic observation of high-order aberrations. The appearances of keratoconus are not symmetric, either rotationally or elliptically. Although a single reflex image of a kerataconic eye may seem to be normal, the 13-image color map shows clear indications of irregularity. About two-thirds of our measured keratoconus eyes show very typical and unique appearance. The BCVA of these keratoconus eyes are normally in the range of 20/20–20/40. Figure 9a shows a result of such a typical type of keratoconus eye image. This measurement was acquired from a young African-American. Although he does suffer from slight monocular diplopia and glare, his vision on both eyes is 20/20. The patient uses only regular spectacles for correction. The presented measurement was obtained from his right eye with manifest refraction of −0.25DS + 3DCX008 (20/20). In the gray-scaled map on the left, the so-called retinoscopic scissors reflex can be observed. When the infrared source was illuminated from the lower side, a shadow could be seen in the middle area surrounded by brighter upper and lower sections, resembling the opened blades of a pair of scissors. When the illumination was coaxial, the brighter sections close up. For upper illumination, the brighter area at the middle area becomes more intense and the upper and lower sections become darker, resembling the closing-up of the scissors blades.

Severe keratoconus cases cannot be missed in any image of the retinoscopic measurement although they look normal to our eyes. The appearances of these cases are very disturbing from the infrared raw images, and they normally render clearly protruding features. Their best corrected visual acuity are typically worse than 20/50. Shown in Figure 9b is one result of the severe KC cases obtained from the left eye of a 28 year-old male with BCVA of 20/80. Severe keratoconus eyes are more difficult to measure with wavefront aberrometry. Although we have eight severe keratoconus eyes, no wavefront aberrometer measurement was available for computational study and comparison.

In our experiment, we imaged many post-LASIK eyes and they present a unique feature in the infrared retinoscopic images. Figure 9c demonstrates a typical case of eyes after LASIK procedures. The image was obtained from an eye 15 months after the bladeless LASIK was performed. The refraction of this eye is −0.50 + 1.00X155 (20/20). The gray-scale map on the left shows clean reflexes in all meridians except a small superficial punctate keratopathy near the center. Notably, the interesting brightness change occurs along the peripheries in all reflex images. The pupil diameters in these reflex images are about 7.1 mm. For the color map on the right, the rotationally symmetric pattern is observed similar to the emmetropic eye images that were demonstrated in Figure 5a, with exception of the peripheral area. The increase of the spherical aberration in LASIK eyes is common and is especially apparent for larger pupil size.

We were able to use the existing wavefront data of the eyes with high-order aberrations to simulate and predict the infrared device's performance and to understand the influence and significance of various ocular factors on the measurement. Figure 10 shows comparison between computation and experiment in two keratoconus eyes with 20/25 BCVA. Figure 10a shows a simulation result of a young eye with manifest refraction of −0.50 + 3.25X155. The small pupil diameter of 4.25 mm in the computation was limited by the wavefront data available. The experiment-measured image of the same eye is presented in Figure 10b. The pupil diameter is about 4.5 mm in this measurement. Figure 10c and (d) shows the result of a second keratoconus eye with manifest refraction of −3.25DS + 3.00DCX10 (20/25-). The pupil diameters in the computation and the experiment are 6 and 7 mm, respectively. The differences in pupil size, gazing direction, and accommodation are some factors that contribute to the discrepancy between the experimental measurement and the computational result that is based solely on the patient's wavefront measurement. The prediction appeared to be excellent under the same conditions of intraocular scattering. However, additional accommodation power was added in this simulation. During the measurement, the patient sees a rapid sequence of soft blinking lights from the near-infrared LED light source panel that is located about 30 cm in front of their eyes. For a hyperopic or a mild myopic eye, accommodation is induced toward the required 3.3 diopters to see clearly those blinking lights. For this particular young eye with refractive prescription of −0.50+3.25X155, a value of +2 diopters was assumed in the computation. Without this accommodation, the measured reflex images could not be reproduced in the simulation.

Figure 11 shows the computational result of a measurement on a 42 year-old normal eye that had a LASIK procedure 5 years before. The manifest refraction of this eye was measured as −1.00DS + 0.75X105 (20/20). The pupil diameter of the wavefront data is 6.75 mm, which is large enough to show clearly the spherical aberration in the periphery. Figure 11b shows the experiment measured image of the same eye. The pupil diameter is about 6.1 mm, which shows less of the periphery, in this measurement. The spherical aberration in the periphery is less pronounced due to the smaller pupil size.

Figure 9. (**a**) Example of a typical keratoconus eye images. Manifest refraction was measurement as RE-0.50DS + 1.50DCX003 and BCVA of 20/20. Scissors reflexes are evident. (**b**) Gray-scale and color maps of a severe case of keratoconus. Manifest refraction was measurement as −6.00DS + 5.00DCX115 (20/80). (**c**) Image of a typical case of LASIK eye. Manifest refraction is measured as −0.50 + 1.00X155 (20/20).

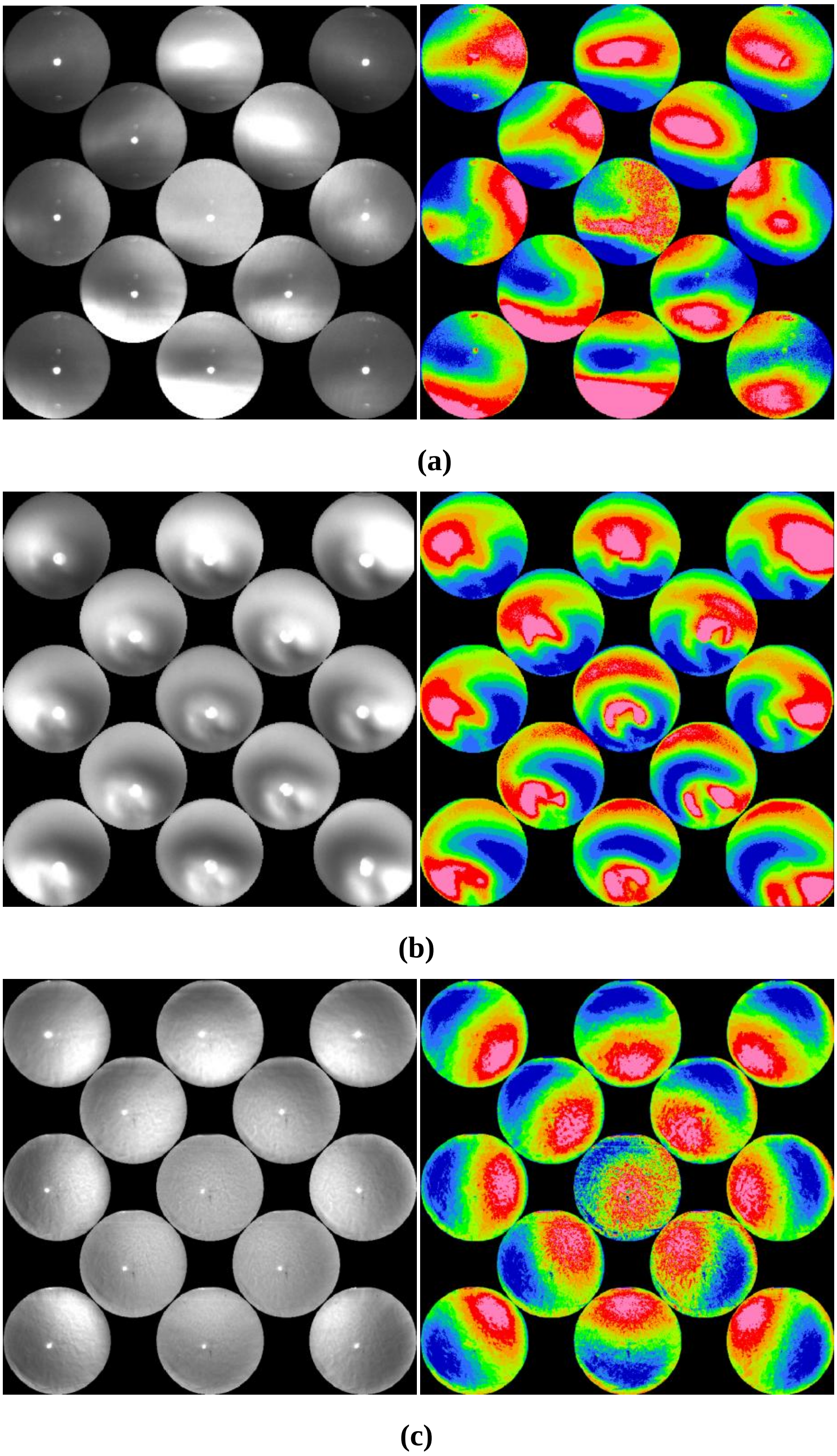

Figure 10. (**a**) Computer simulation result of infrared retinoscopy measurement on a 28 year-old keratoconus eye using a paraxial eye model with the customer wavefront data. The manifest refraction of this eye was measured as −0.50DS + 3.25DCX155 (20/25). The pupil diameter of the wavefront data is 4.25 mm. Two diopters of accommodation was assumed in the computation. (**b**) The experimental-measured image of the same eye. The pupil diameter is about 4.5 mm in this measurement. (**c**) Computation result of a 35 year-old keratoconus eye. The manifest refraction was measured as −3.25DS + 3.00DCX10 (20/25-). The pupil diameter of the wavefront data is 6 mm, and 2.1 diopters of accommodation was assumed in this computation. (**d**) The experimental-measured image of the same eye. The pupil diameter is about 6.9 mm in this measurement.

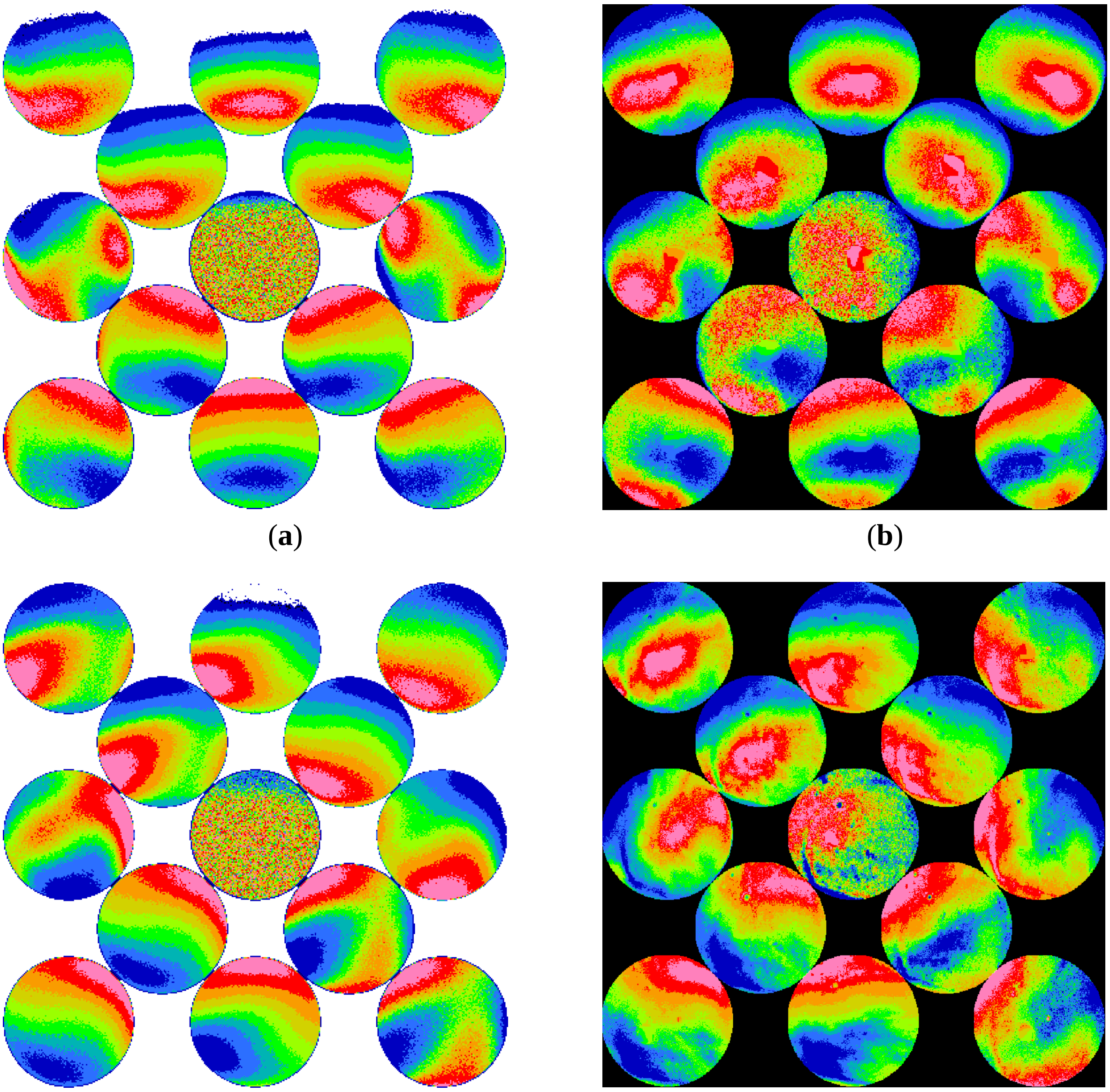

(**a**) (**b**)

(**c**) (**d**)

Figure 11. (**a**) Computer simulation result of infrared retinoscopy measurement on a 42 year-old normal eye that had LASIK procedure 5 years before. The manifest refraction of this eye was measured as −1.00DS + 0.75X105 (20/20). The pupil diameter of the wavefront data is 6.75 mm, which is large enough to show clearly the spherical aberration in the periphery. (**b**) The experiment measured image of the same eye. The pupil diameter is about 6.1 mm in this measurement.

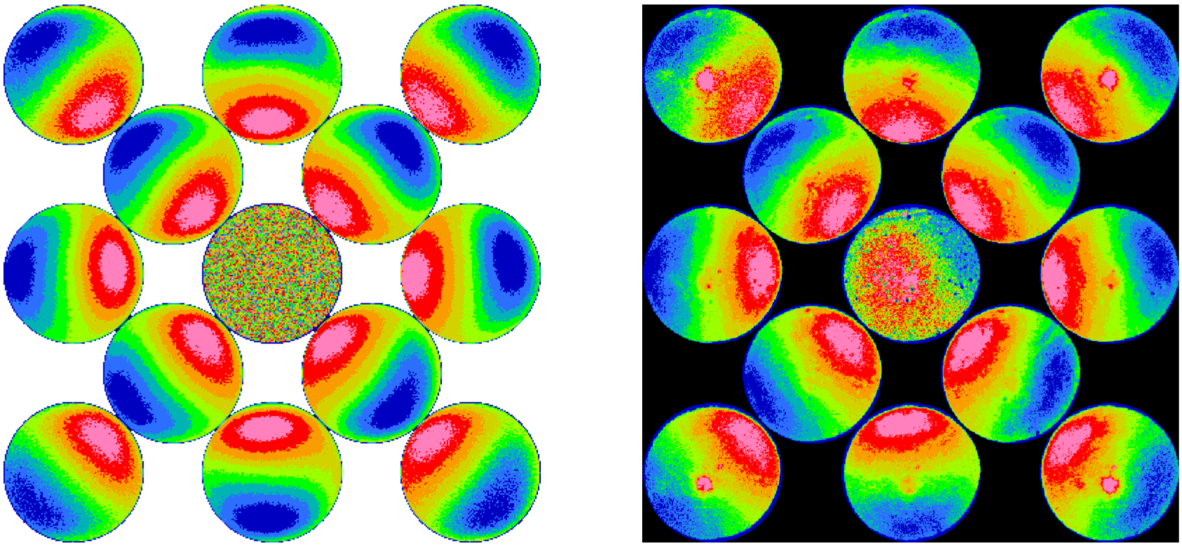

(**a**) (**b**)

5. Conclusions

Through experiment and computation, this paper discusses and demonstrates the ophthalmic measurements with an infrared retinoscope. The retinoscopic pupil reflex images of several different conditions are presented in direct photographs and enhanced color images. Digitization of images and simple image analysis algorithms greatly improve the visualization. As the results show, small optical defects could be observed from the direct- or back-scattered light similar to the direct- and retro-illuminations of a slit lamp. Low- and high-order ocular aberrations appear as the background to the small optical defects. The type of aberration presents itself with shadows and intensity gradient variations of the pupil reflex. Defocus, astigmatism, and high-order aberrations in keratoconus and LASIK eyes show unique appearances of their own and can be identified easily.

Disregarding the possible discrepancy in pupil size, direction of gaze, and accommodations, the computation results show agreement with experiment results. Our computation indicates that the retinal stray light or intraocular scattering plays an important role for the far eccentric detection in retinoscopy. The simulations results from tested eyes suggest that the retinal stray light that is strongly linked to intraocular scattering extend the detection range of illuminating eccentricity in retinoscopy and make it more likely to observe ocular aberrations.

Acknowledgments

The authors would like to thank the reviewers for their extensive efforts and valuable advices. This research project was partially supported by the Center for Laser Applications of the University of

Tennessee Space Institute and the support for eye modeling and keratoconus research of the National Eye Institute grants R21 EY18385 and R21 EY018935 respectively.

Author Contributions

Ying-Ling Chen wrote the manuscript with edits performed by J. W. L. Lewis. Ying-Ling Chen performed the optical computation. Lei Shi developed the hardware prototype and image analysis codes. Ying-Ling Chen and Lei Shi performed clinical testing and data collection. Ming Wang and Wang Vision Institute supervised the safety in clinical testing. Ying-Ling Chen, J. W. L. Lewis, and Ming Wang were responsible for the design of the research and the funding of the project.

Conflicts of Interest

Ying-Ling Chen and J. W. L. Lewis are the inventors of the related US patents # 7.427.135, 7,878.652, and 8.403.480, entitled Adaptive Photoscreen System. J. W. L. Lewis and Ming Wang are the inventors of a pending patent entitled Adaptive Infrared Retinoscopic Device for Detecting Ocular Aberrations. Lei Shi declares no conflict of interest.

References

1. Corboy, J.M. *The Retinoscopy Book−A Manual for Beginners*; SLACK: New Jersey, NJ, USA, 1984.
2. Millodot, M. A centenary of retinoscopy. *J. Am. Opt. As.* **1973**, *44*, 1057–1059.
3. Nagy, Z.Z.; Suveges, I.; Senyi, K. Hatos, E.; Fust, A. Retinoscopy after excimer laser photorefractive treatments. *Acta Chir. Hung* **1995**, *35*, 307–313.
4. Mutti, D.O. Sources of normal and anomalous motion in retinoscopy. *Optom. Vis. Sci.* **2004**, *81*, 663–672.
5. Tan, B.; Chen, Y.L.; Baker, K; Lewis, J.W.L.; Swartz, T.; Jiang, Y.; Wang, W. Simulation of realistic retinoscopic measurement. *Opt. Exp*. **2007**, *15*, 2753–2761.
6. Kaakinen, K. A simple method for screening of children with strabismus, anisometropia or ametropia by simultaneous photography of the corneal and the fundus reflexes. *Acta Ophthalmol.* **1979**, *57*, 161–171.
7. Bobbier, W.R.; Braddick, O.J. Eccentric photorefraction: optical analysis and empirical measures. *Am. J. Optom. Physiol. Opt.* **1985**, *62*, 614–620.
8. Howland, H.C. Optics of photoretinoscopy: Results from ray tracing. *Am. J. Optom. Physiol. Opt.* **1985**, *62*, 621–625.
9. Howland, H.C. Photorefraction of eyes: History and future prospects. *Optom. Vis. Sci.* **2009**, *86*, 603–606.
10. Caballero, M.T.; Furlan, W.D.; Pons, A.; Saavedra, G.; Martinez-Corral, M.; Detection of wave aberrations in human eye using a retinoscopy-like technique. *Opt. Comm.* **2006**, *260*, 767–771.
11. Roorda, A.; Campbell, M.C.; Bobier, W.R. Slope-based eccentric photorefraction: Theoretical analysis of different light source configurations and effects of ocular aberrations. *J. Opt. Soc. Am. A Opt. Image Sci. Vis.* **1997**, *14*, 2547–2556.

12. Chen, Y.L.; Tan, B.; Lewis, J.W. Simulation of eccentric photorefraction images. *Opt. Express.* **2003**, *11*, 1628–1642.
13. Ven den Berg, T.J.; Franssen, L.; Kruijt, B.; Coppens, J.E. History of ocular straylight measurement: A review. *Z Med. Phys*. **2013**, *23*, 6–20.